Thin Solid Films 709 (2020) 138165

Contents lists available at ScienceDirect

Thin Solid Films

journal homepage: www.elsevier.com/locate/tsf

Low-loss GeO_2thin films deposited by ion-assisted alternating current reactive sputtering for waveguide applications

J.W. Miller[a,*], M. Chesaux[b], D. Deligiannis[b], P. Mascher[a], J.D.B. Bradley[a]

[a] Department of Engineering Physics and Centre for Emerging Device Technologies, McMaster University, 1280 Main Street West, Hamilton, Onatrio L8S 4L7, Canada
[b] Intlvac, 247 Armstrong Avenue, Unit 6, Halton Hills, Ontario L7G 4X6, Canada

ARTICLE INFO

Keywords:
Reactive sputtering
Germanium oxide
Thin film
Optical loss
Photonics
Dual alternate current sputtering
Waveguide

ABSTRACT

We report low optical loss germanium oxide (GeO_2) thin films which have been deposited by low pressure ion-assisted alternating current dual magnetron sputtering of germanium targets in an oxygen plasma environment. The germanium oxide films ranging from 0.7- to 1.0-μm-thick were fabricated at low temperature and high deposition rates of 6–38 nm/min on silicon and thermally oxidized silicon substrates. The refractive index of the films was determined through variable angle spectroscopic ellipsometry and found to be 1.6051 on average at a wavelength of 638 nm. The films were shown to be near stoichiometric through Rutherford backscattering spectroscopy analysis and displayed sub-nanometer roughness when measured with atomic force microscopy. High peak-to-valley uniformity on a 3-inch substrate with relative deviation of 0.8% was achieved. We characterized the attenuation of the GeO_2 thin films from visible to near-infrared wavelengths and observed it to be as low as 0.1 dB/cm at 638 nm for deposition rates of 8 nm/min. This deposition technique provides complementary metal-oxide-semiconductor compatible GeO_2 thin films suitable for integrated photonics applications and is promising for the fabrication of other dielectric waveguide materials.

1. Introduction

Germanium oxide (GeO_2) is a material that is widely used in photonic applications because of its advantageous structural and optical properties. GeO_2 first gained interest in its applications in doped optical fibers due to its structural similarities to silica, allowing for ease of integration into fiber cores [1]. GeO_2 glass has strong inter-ionic forces between the Ge^{4+} and O^{2-} ions which provide high thermal stability and mechanical strength [2]. It has a higher refractive index (n = 1.6) than silica and is used to increase the numerical aperture of optical fibers. GeO_2 possesses a high Raman gain coefficient when compared to other oxide-based glasses [3], making it a strong candidate for Raman based amplification. It also shows promise as a host for rare earth dopants amplifiers and lasers due to its high rare-earth solubility [4]. Its low nonlinearity and absorption allow for long-distance optical transmission in fibers [5]. GeO_2 glass possesses strong opto-refractive effects allowing for permanent shifts in refractive index when exposed to UV radiation [4–7]. This property is used to write Bragg gratings in optical fibers by UV laser exposure for applications, including fiber lasers, sensors, and dispersion compensators [8–11].

GeO_2's high refractive index and low loss also make it a promising material for planar waveguide applications. Because it is a complementary metal-oxide-semiconductor compatible material already extensively used in silicon foundries for high-k gate dielectrics [12,13], it is particularly attractive for silicon photonics platforms [14]. Its high rare-earth (RE) solubility motivates its use in on-chip amplifiers and lasers. Optical gain and lasing have been demonstrated in germanosilicate glass [15] and several authors have reported efficient photoluminescence in RE-doped germinate alloys such as lead-, antimony-, and bismuth-germinate glasses [16–20]. The UV sensitivity of GeO_2 suggests it might be useful for grating structures or as a UV-sensitive cladding material for post-process trimming to increase yield in silicon photonics devices [21].

While the physical and material properties of GeO_2 thin films have been explored, there has been limited investigation towards the fabrication of low loss thin films. GeO_2 thin films have been previously fabricated by radio frequency (RF) sputtering and reactive direct current (DC) sputtering [2, 22–24]. Both of these techniques have been able to achieve high deposition rates; however, they have not been able to produce films with as-deposited losses of less than 1.9 dB/cm at 638 nm. The losses in these films have been reduced by post-deposition annealing or laser annealing, which adds processing steps and increases fabrication complexity [2]. Germanate based alloy waveguide structures have achieved losses ranging from around 0.6 to 2.2 dB/cm at

* Corresponding author.
E-mail address: millej29@mcmaster.ca (J.W. Miller).

https://doi.org/10.1016/j.tsf.2020.138165
Received 12 November 2019; Received in revised form 29 May 2020; Accepted 1 June 2020
Available online 06 June 2020

632 nm, with these losses being attributed to scattering off of the waveguide sidewalls [25,26].

Alternating current (AC) dual magnetron sputtering in conjunction with high energy ionic bombardment is known to yield high-quality thin films with high density and uniformity [27]. While other films such as magnesium oxides and tantalum oxynitrides have been fabricated and reported on for optical applications [28,29], GeO_2 thin film fabrication has not been extensively explored using this deposition technique.

In this paper, we study GeO_2 thin film deposition using ion assisted AC dual magnetron sputtering. We deposit the films in varying regions of the sputtering hysteresis bias curve and study their structural and optical properties. The film stoichiometry is confirmed through high energy ion-matter interactions using Rutherford backscattering spectrometry (RBS) and elastic recoil detection analysis (ERDA). We measure low propagation losses using the prism coupling technique and observe low surface roughness using atomic force microscopy (AFM). These properties, combined with high deposition rates and insensitivity to process variation, demonstrate ion-assisted AC dual magnetron sputtering to be a highly promising method for planar waveguide fabrication.

2. Experimental methods

2.1. Ion-assisted AC dual magnetron sputtering of GeO_2 thin films

We deposited the GeO_2 thin films using an Intlvac Nanocrhome IV Plasma Assisted Reactive Magnetron Sputtering (PARMS) system. A schematic of the system is displayed in Fig. 1. The tool is a top-down sputter system that can be equipped with up to four 6″ sputter sources for pulsed DC or dual AC sputtering. In addition, the system contains an ion source for in-situ pre-cleaning and ion-assisted deposition. The PARMS system is designed for the production of dense and low defect films. Prior to the deposition, the chamber was pumped down to 1.3×10^{-7} kPa with a cryopump. Subsequently, the films were deposited under low heating, at 120 °C, using two 6-inch 99.995% pure germanium targets. The plasma processing parameters were varied across oxygen flow ranging from 40 to 80 standard cubic centimeters per minute (sccm) at constant power. In order to maintain film homogeneity during the growth process, the oxygen flow was either held constant or adjusted by an algorithm to maintain a selected target bias. In order to select the deposition parameters across different sputtering regimes, the target bias response for the system was examined. The target bias vs. O_2 flow rate hysteresis curves are shown in Fig. 2. The transition from metal to poisoned target mostly takes place between 40 and 65 sccm of O_2 flow. The difference between the curve when transitioning from oxide to metal and vice-versa are likely the result of slow variation in the chamber wall and target surface condition [30]. Films were deposited on either side of the hysteresis, i.e. where the target bias is relatively insensitive to oxygen flow and the process is inherently stable, as well as inside the hysteresis, e.g. at 550 V where the algorithm is necessary to stabilize it [31]. The films were deposited on ⟨100⟩ silicon wafers for compositional analysis, as well as silicon substrates with 6-μm-thick thermal oxide for waveguide characterization, all fixed to a rotating sample holder.

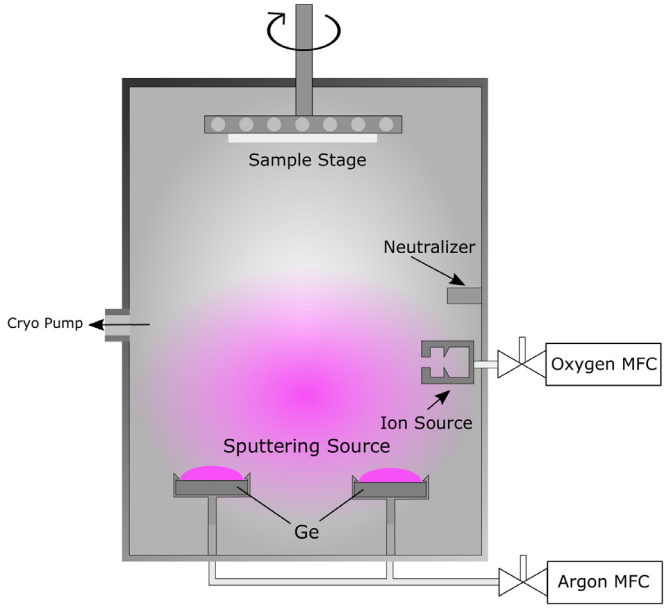

Fig. 1. Schematic of the ion-assisted dual AC sputtering system applied to deposit GeO_2 thin films. The position of the ion source and neutralizer are not representative of the actual position and the system is not drawn to scale.

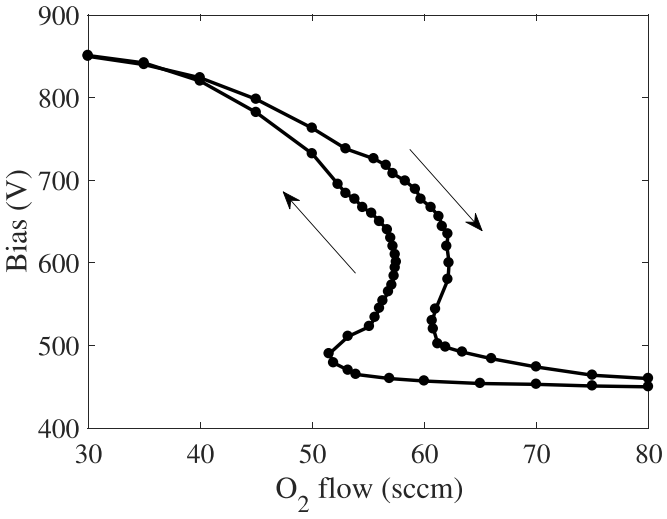

Fig. 2. Target bias hysteresis for varying oxygen flow under ion-assisted deposition.

2.2. Thin film characterization

We determined the composition of the GeO_2 films using RBS and ERDA. The RBS results were collected using a 1.8 MeV $^4He^+$ ion beam in a Cornell geometry with a dose of 2 μC. The sample underwent random rotation during data acquisition to limit the effects of channeling in the crystalline silicon substrate. The ERD results were collected with a 2.9 MeV $^4He+$ ion beam with an incident and exit angle of 75° to the normal of the sample surface. Modeling of the experimental data was performed using the SIMNRA software package to determine the stoichiometric composition of the thin films [32].

We determined the thicknesses and refractive indices of the thin films with the use of a J. A. Woollam M-2000 UV–Vis variable angle spectroscopic ellipsometer (VASE) fitted with a near-infrared extension. Measurements in the spectral range of 250 to 1700 nm were taken at angles of 55°, 60°, 65°, 70°, and 75° from the surface normal. The spectra were then analyzed with the use of J. A. Woollam's CompleteEASE™ software package, assuming a homogenous film comprised of a single layer with no surface roughness on a silicon substrate [33].

In order to determine the optical loss of the deposited material, a set of 0.7-μm-thick films were grown onto 6-μm-thick thermal oxide layers on 3″ diameter Si wafers. The propagation loss of the films deposited on oxidized silicon wafers was measured using a Metricon 2010/M prism coupler at 638, 847 and 1550 nm wavelength. Using a set of linear polarizers, the light was coupled into the film under transverse electric (TE) and transverse magnetic (TM) mode conditions. The mode order was selected by altering the coupling angle of the incident laser onto

the prism with the fundamental TE and TM modes being chosen. Measurements were performed across different regions of the wafer approximately ten times and the statistical average of these measurements was selected as the loss of the film. We carried out multiple measurements to account for the sensitivity of the prism coupling system to the scattering of the propagating light from surface defects along the beam path. Pieces of the GeO_2-coated oxide oxidized Si wafers were cleaved and annealed separately in an annealing furnace under a constant N_2 gas flow of 60 sccm. The samples were annealed at temperatures ranging from 200 to 400 °C in steps of 50 °C.

The surface roughness of 1.0-μm-thick films on polished silicon was measured using AC mode AFM. A probe stiffness of 60 N/m and a frequency of 300 kHz was used. Three random 2 μm x 2 μm locations on the surface were measured to determine the average root mean squared (RMS) roughness of the film. This scan size was significantly larger than the surface features, thus was determined to be sufficiently large to obtain an average roughness. The data analysis for the AFM measurements was performed in the WSXM 5.0 application [34].

3. Results and discussion

Fig. 3(a) shows the experimental RBS spectra and corresponding simulated fit for a GeO_2 thin film grown with an O_2 flow rate of 60 sccm. A single layer model for the deposited film consisting of germanium, oxygen, and silicon was applied to the experimental data. There is no evidence of interstitial argon in the films based on a lack of signal around 1000 keV. From the fitted models, it can be observed that the films are near stoichiometric GeO_2 within the experimental uncertainty for germanium of 0.1 atomic% and oxygen of 0.8 atomic%. This uncertainty is obtained through the fit statistics given by the SIMNRA software. The lower uncertainty in the atomic percentage of germanium compared with oxygen can be attributed to germanium's higher atomic mass, which results in a larger atomic cross-section and a higher probability of scattering incoming He^+ ions. This stronger scattering renders the concentration of heavier elements more sensitive to measurement. The composition of the GeO_2 thin films does not change for different oxygen flow rates operating in the poisoning regime for the Ge targets as well as the metal sputtering regime and the hysteresis midpoint.

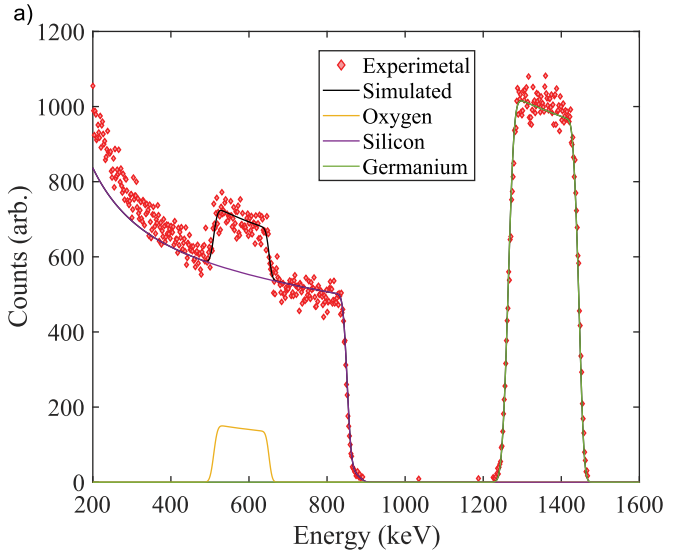

Fig. 3. a) RBS experimental spectra (red dots) and fits based on a simulation model for a GeO_2 thin film. The yellow, purple, and green fit lines represent oxygen, silicon, and germanium, respectively. The composition of the GeO_2 is stoichiometric within the uncertainty in the simulated model. b) ERDA experimental spectra (red dots) with fit based on simulation model for 1.1 at.% hydrogen content uniformly distributed throughout the film.(For interpretation of the references to color in this figure legend, the reader is referred to the web version of this article.)

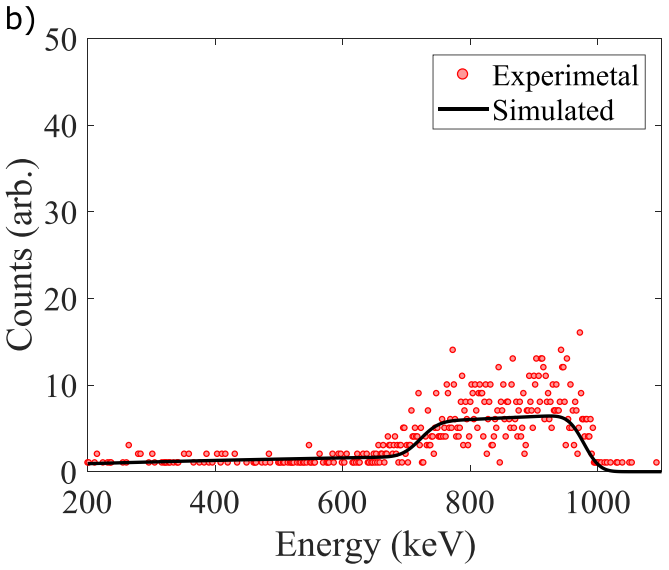

Fig. 3. (*continued*)

Fig. 3(b) shows the ERDA spectrum measured for the same GeO_2 film in order to characterize the hydrogen content. The simulated model suggests a hydrogen concentration of 1.1 at.% spread evenly throughout the thickness of the film. The source of this hydrogen is not certain. A possible explanation is the instruction of hydrogen into the chamber from residual water vapor which is then incorporated into the film during the deposition. Alternatively, the hydrogen in the film might arise from water vapor diffusing into the film between deposition and ERD measurements. We note that the presence of hydrogen in the films can be useful for specific applications. It is proposed that the presence of OH groups can contribute to defect sites such as germanium electron trap centers and these centers contribute to the photorefractive properties of GeO_2 when exposed to UV light [35,36].

The Cauchy and Sellmeier model were applied to characterize the dispersion properties of the GeO_2 thin films from data obtained through VASE. The film loss was characterized using the Urbach absorption model. For this model, the parameters of the silicon substrate were taken from Herzinger [37]. Fig. 4(a) shows the Cauchy dispersion model and Urbach absorption as well as the Sellmiere model for a 60-

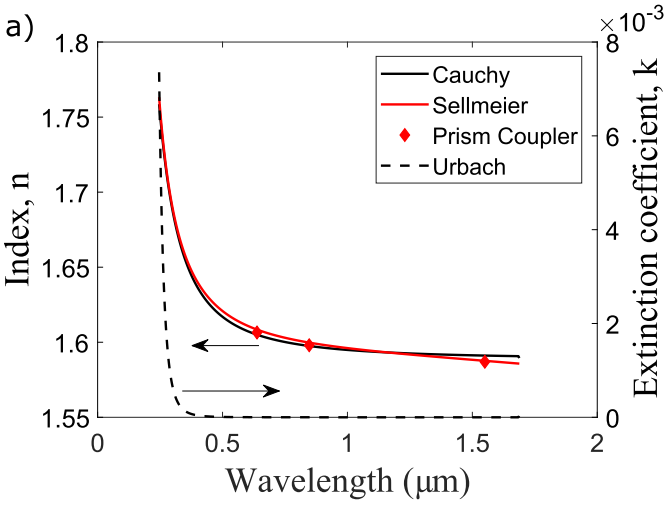

Fig. 4. a) Material dispersion of GeO_2 thin film deposited with 60-sccm O_2 flow measured with VASE and prism coupler. b) Height of GeO_2 thin film in nm using the Cauchy model measured across 3 inch silicon wafer.

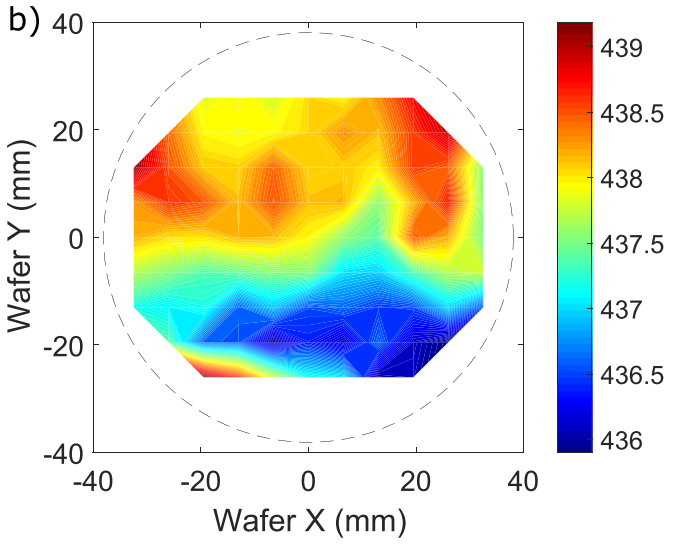

Fig. 4. (*continued*)

sccm O_2 flow GeO_2 film. Overlaid on top of the dispersion curves are direct refractive index measurements obtained using prism coupling at three separate wavelengths. These overlap with the Cauchy and Sellmeier dispersion model except for the measurement taken at 1550 nm in which the Cauchy model overestimates the index. This difference is expected as the Sellmeier model is considered better over large wavelength ranges. The Cauchy model serves as a reasonable approximation across the visible region and is defined by the three-term function:

$$n = A + B\lambda^{-2} + C\lambda^{-4} \quad (1)$$

where the fitting parameters *A, B* and *C* are the material-dependent Cauchy coefficients, *n* is the refractive index of the film and λ is the wavelength. Likewise, a 2-term Sellmeier model was used given by the formula:

$$n^2 = \varepsilon(\infty) + \frac{B_1\lambda^2}{\lambda^2 - C_1^2} - E\lambda^2 \quad (2)$$

where $\varepsilon(\infty)$ is the index offset, B_1 and C_1 are the experimentally determined Sellmeier coefficients and *E* is the position of the pole in the infrared. The values for the dispersion models shown in Fig. 4 are presented in Table 1. The refractive indices reported here are similar to those reported elsewhere using other deposition techniques [2,23]. Fig. 4b) shows the height map of a 3-inch silicon wafer coated in GeO_2 positioned mid-way between the center and the edge of the sample stage. The film shows high uniformity across a large area with a relative deviation in thickness (Max-Min)/average of 0.8% across the 437.7 nm thick GeO_2 thin film with a standard deviation from the mean of 0.2%.

Sputtering at lower oxygen flow rates resulted in a significant increase in the deposition rate, from 8 to 10 nm/min at flow rates of greater than 60 sccm to 38 nm/min at 40 sccm, as shown in Fig. 5(a). This increase in deposition rate primarily can be attributed to the lower O_2 partial pressure, reducing target surface oxidation, thus increasing the germanium sputtering probability at lower O_2 flow rates [31]. There a noticeable trend in the thin film losses deposited at different

Table 1
Cauchy and Sellmeier dispersion parameters coefficients obtained through VASE.

Cauchy	A	B (μm) $^{-2}$	C (μm) $^{-4}$	
	1.587	6.310 $\times 10^{-3}$	2.278 $\times 10^{-4}$	
Sellmeier	$\varepsilon(\infty)$	B_1 (μm) ^{2}	C_1 (μm) ^{2}	E (μm) $^{-2}$
	1.665	8.63 $\times 10^{-1}$	1.5447 $\times 10^{-1}$	8.84 $\times 10^{-3}$

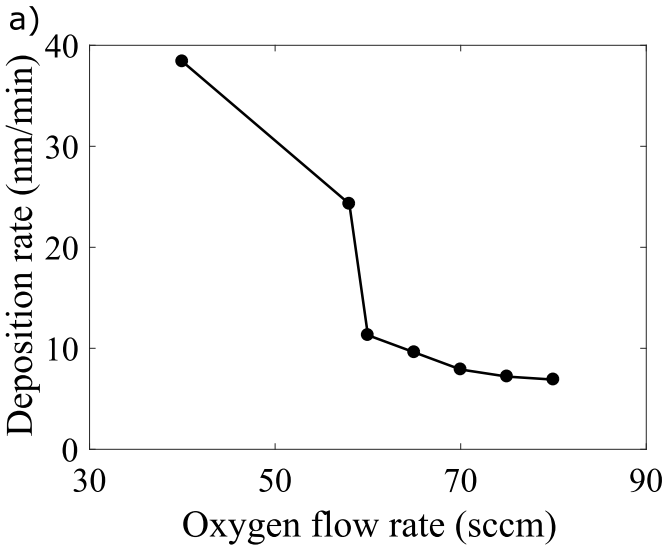

Fig. 5. a) GeO_2 thin film deposition rate vs. O_2 flow rate under ion-assisted growth. b) As deposited film loss at 638 nm measured by the prism coupling method of TE mode light vs. deposition rate. Insert shows 638 nm red streak from prism coupler coupling into GeO_2 film.

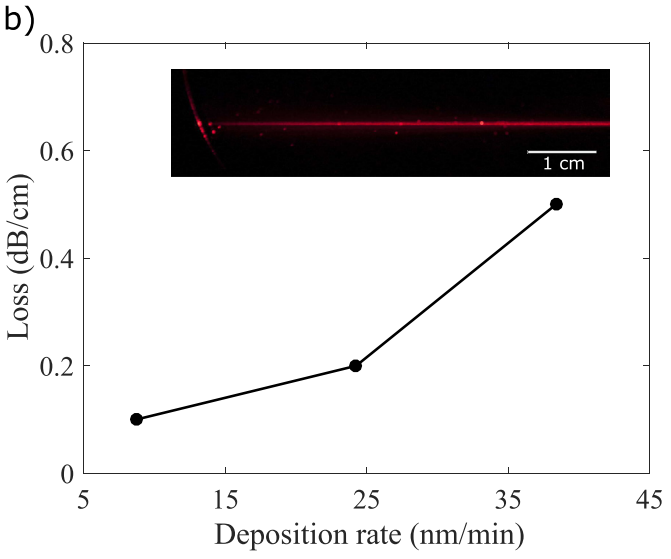

Fig. 5. (*continued*)

deposition rates. Those films deposited at lower rates in the poisoned regime showed low losses that were at the measurement limit of 0.1 dB/cm at 638 nm across the wafer for both the fundamental TE and TM modes. Films that were grown in the knee of the hysteresis with deposition rates around 25 nm/min showed losses around 0.2 dB/cm at 638 nm, and films grown in the metal sputtering region showed losses around 0.5 dB/cm at 638 nm, for both the fundamental TE and TM modes.

AFM was used to study whether surface roughness could account for the higher losses at 638 nm seen in the films with higher deposition rates. The RMS surface roughness of films deposited with between 60 and 80 sccm of O_2 and with deposition rates below 10 nm/min was typically 0.5 to 0.8 nm. This is consistent with other films grown through PARMS [38]. Annealing selected films in the range of 200 to 400 °C, as shown in Fig. 6, did not yield a noticeable difference in roughness compared to the as-deposited films. It can be noted that there appears to be a correlation between surface roughness and loss, shown in Table 2. The film with an RMS surface roughness of 0.92 nm exhibited the highest loss with 0.5 dB/cm at 638 nm. Conversely, the film

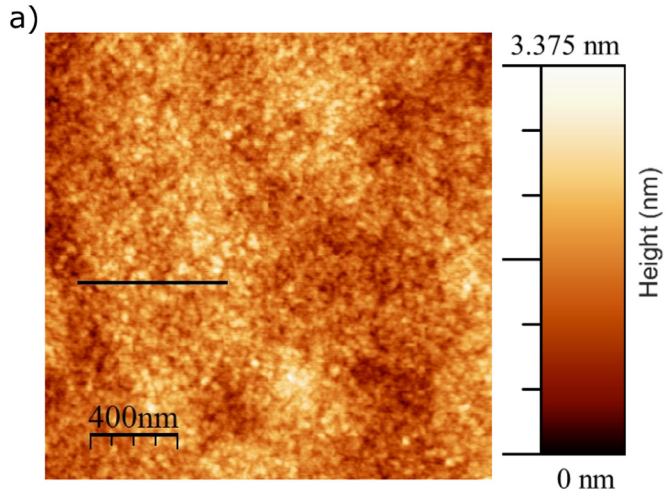

Fig. 6. a) AFM profile for a 1-μm-thick GeO_2 thin film annealed at 400 °C with RMS roughness of 0.45 nm and peak to peak roughness of 3.8 nm. b) Height profile taken from AFM scan in a).

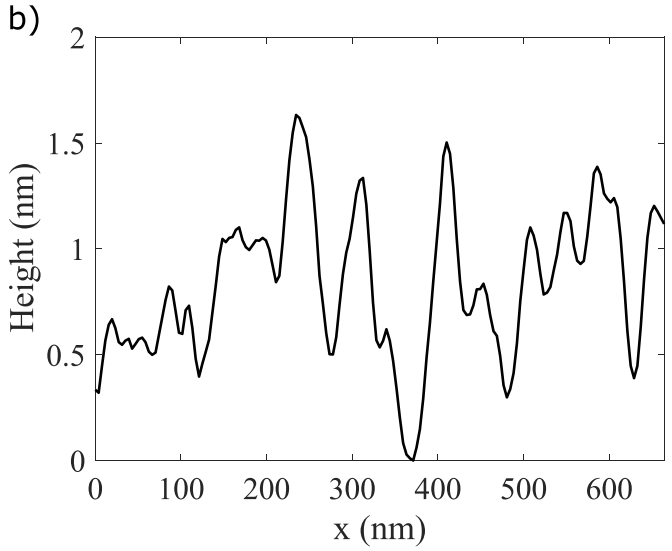

Fig. 6. (*continued*)

Table 2
Deposition parameters, atomic concentrations obtained through RBS, refractive index obtained through VASE, RMS roughness and peak to peak roughness for films obtained through AFM, losses obtained from prism coupling.

O_2 flow rate (sccm)	Ge (at. % ± 0.1)	O (at. % ± 0.8)	N @ 638 nm	Loss, 638 nm (dB/cm)	R_{RMS} (nm)	Peak to Peak (nm)
40	31.0	69.0	1.603	0.5	0.92	9.2
55	31.0	69.0	1.600	0.2	0.73	6.2
60	32.5	67.5	1.605	0.1	0.54	4.1
65	32.5	67.5	1.605	–	0.53	5.1
70	32.8	67.2	1.605	–	1.21	8.6
75	33.0	67.0	1.605	–	0.77	8.9
80	32.8	67.2	1.605	–	0.45	3.8

with an RMS surface roughness of 0.54 nm had the lowest loss of 0.1 dB/cm at 638 nm. The loss in these films appears to decrease at higher wavelengths with all of them measuring a loss at 0.1 dB/cm at a wavelength of 980 nm. Given that scattering is scaled as λ^{-4}, we would expect the loss decrease at higher wavelengths if the primary loss mechanism was caused through light scattering at the interfaces.

The RMS roughnesses of the as-deposited films are less than those of similar GeO_2 films grown by RF magnetron sputtering [23] and DC reactive sputtering [22]. Thin films grown using PARMS have been shown to exhibit high packing densities and film surface uniformity [38]. The losses in these GeO_2 films are also shown to be less than the films grown using other methods without the need for post-processing.

4. Conclusions

We have demonstrated low-loss GeO_2 thin films fabricated by PARMS AC sputtering and show an improvement in losses for the as-deposited GeO_2 films compared to previous deposition techniques. The films were shown to be stoichiometric through RBS measurements, and the refractive index was modeled through VASE and prism coupler measurements and determined to be around 1.605 at 638 nm. The film composition and refractive index were found to be constant for different O_2 flow rates. Small amounts of hydrogen were present in the films, which might not be considered detrimental as hydrogen is known to sensitize GeO_2 to change its refractive index through the photorefractive effect. The films were shown to have sub-nanometer surface roughnesses down to 0.5 nm, as determined through AFM, and losses as low as 0.1 dB/cm at 638 nm without the need for post-deposition process steps. The films also had high uniformity across a 3-inch wafer with a relative thickness deviation of 0.8%. The low surface roughnesses and losses demonstrate ion-assisted dual AC sputtering to be especially attractive for the deposition of optical waveguide materials.

CRediT authorship contribution statement

J.W. Miller: Methodology, Formal analysis, Writing - original draft, Writing - review & editing. **M. Chesaux:** Methodology, Writing - original draft. **D. Deligiannis:** Resources, Funding acquisition. **P. Mascher:** Supervision, Writing - review & editing. **J.D.B. Bradley:** Supervision, Writing - review & editing.

Declaration of Competing Interests

None.

Acknowledgments

The authors would like to acknowledge Lyudmila Goncharova and Jack Hendriks from Western University's Tandetron Laboratory for their assistance with RBS and ERD measurements as well as Liam Pasinato with his assistance with VASE measurements. The authors would also like to acknowledge the Center of Emerging Device Technology for their equipment and recourses.

References

[1] P.J. Lemaire, A.M. Vengsarkar, W.A. Reed, D.J. DiGiovanni, Thermally enhanced ultraviolet photosensitivity in GeO_2 and P_2O_5 doped optical fibers, Appl. Phys. Lett. 66 (1995) 2034–2036, https://doi.org/10.1063/1.113683.
[2] S. Valligatla, A. Chiasera, N. Bazzanella, L. Lunelli, A. Miotello, M. Mazzola, D.N. Rao, M. Ferrari, CO_2 Laser irradiation of GeO_2 planar waveguide fabricated by rf-sputtering, IOP Conf. Ser. Mater. Sci. Eng. 73 (2015) 1537–1545, https://doi.org/10.1088/1757-899X/73/1/012006.
[3] F.L. Galeener, J.C. Mikkelsen, R.H. Geils, W.J. Mosby, The relative Raman cross sections of vitreous SiO_2, GeO_2, B_2O3, and P_2O5, Appl. Phys. Lett. 32 (1978) 34–36, https://doi.org/10.1063/1.89823.
[4] A. Jha, B. Richards, G. Jose, T. Teddy-Fernandez, P. Joshi, X. Jiang, J. Lousteau, Rare-earth ion doped TeO_2 and GeO_2 glasses as laser materials, Prog. Mater. Sci. 57 (2012) 1426–1491, https://doi.org/10.1016/j.pmatsci.2012.04.003.
[5] E.M. Dianov, V.M. Mashinsky, Germania-based core optical fibers, J. Light. Technol. 23 (2005) 3500–3508, https://doi.org/10.1109/JLT.2005.855867.
[6] S. Sebastiani, G.N. Conti, S. Pelli, G.C. Righini, A. Chiasera, M. Ferrari, C. Tosello, Characterization of a highly photorefractive RF-sputtered SiO_2-GeO_2 waveguide, Opt. Express 13 (2005) 1696–1701.
[7] J.-.P. Bérubé, A. Le Camus, S.H. Messaddeq, Y. Petit, Y. Messaddeq, L. Canioni, R. Vallée, Femtosecond laser direct inscription of mid-IR transmitting waveguides

in BGG glasses, Opt. Mater. Express 7 (2017) 3124, https://doi.org/10.1364/OME.7.003124.
[8] T. Geernaert, M. Becker, P. Mergo, T. Nasilowski, J. Wojcik, W. Urbanczyk, M. Rothhardt, C. Chojetzki, H. Bartelt, H. Terryn, F. Berghmans, H. Thienpont, Bragg Grating inscription in GeO_2 -doped microstructured optical fibers, J. Light. Technol. 28 (2010) 1459–1467, https://doi.org/10.1109/JLT.2010.2043414.
[9] X. Liu, X. Yang, F. Lu, J. Ng, X. Zhou, C. Lu, Stable and uniform dual-wavelength erbium-doped fiber laser based on fiber Bragg gratings and photonic crystal fiber, Opt. Express 13 (2005) 142, https://doi.org/10.1364/OPEX.13.000142.
[10] A.D. Kersey, T.A. Berkoff, W.W. Morey, Multiplexed fiber Bragg grating strain-sensor system with a fiber Fabry–Perot wavelength filter, Opt. Lett. 18 (1993) 1370, https://doi.org/10.1364/OL.18.001370.
[11] B.J. Eggleton, T. Stephens, P.A. Krug, G. Dhosi, Z. Brodzeli, F. Ouellette, Dispersion compensation using a fibre grating in transmission, Electron. Lett. 32 (1996) 1610, https://doi.org/10.1049/el:19961027.
[12] T. Sato, Y. Otani, H. Toyota, Y. Fukuda, Y. Yazaki, T. Ono, Low-temperature formation of high-quality GeO_2 interlayer for High-K gate dielectrics/Ge by electron-cyclotron-resonance plasma techniques, IEEE Trans. Electron Devices 57 (2009) 282–287, https://doi.org/10.1109/ted.2009.2035030.
[13] B. Rajni, Realization of directional-coupler-based optical waveguide devices by ultraviolet-imprinting technique using sol-gel derived inorganic GeO_2:siO_2 Films, IEEE Photonics Technol. Lett. 19 (2007) 2048–2050.
[14] W. Bogaerts, L. Chrostowski, Silicon photonics circuit design: methods, tools and challenges, Laser Photon. Rev. 12 (2018) 1700237, , https://doi.org/10.1002/lpor.201700237.
[15] J. Hübner, S. Guldberg-Kjaer, M. Dyngaard, Y. Shen, C.L. Thomsen, S. Balslev, C. Jensen, D. Zauner, T. Feuchter, Planar Er- and Yb-doped amplifiers and lasers, Appl. Phys. B. 73 (2001) 435–438, https://doi.org/10.1007/s003400100697.
[16] C.B. de Araújo, L.R.P. Kassab, C. Tolentino Dominguez, S.J.L. Ribeiro, A.S.L. Gomes, A.S. Reyna, Photoluminescence and nonlinear optical phenomena in plasmonic random media—a review of recent works, J. Lumin 169 (2016) 492–496, https://doi.org/10.1016/j.jlumin.2014.11.013.
[17] S.J. Huang, Y.B. Xiao, J.L. Liu, Y. Ji, L.Y. Mao, W.C. Wang, Nd^{3+}-doped antimony germanate glass for 1.06μm fiber lasers, J. Non. Cryst. Solids. 518 (2019) 10–17, https://doi.org/10.1016/j.jnoncrysol.2019.05.008.
[18] D. Manzani, M. Montesso, C.F. Mathias, K.V. Krishanaiah, S.J.L. Ribeiro, M. Nalin, Visible up-conversion and near-infrared luminescence of $Er^{3+}Yb3^{+}$ co-doped $SbPO_4$-GeO_2 glasses, Opt. Mater. (Amst) 57 (2016) 71–78, https://doi.org/10.1016/j.optmat.2016.04.019.
[19] L.R.P. Kassab, D.K. Kumada, D.M. da Silva, J.A.M. Garcia, Enhanced infrared-to-visible frequency upconversion in Yb^{3+}/Er^{3+} codoped Bi_2O3–GeO_2 glasses with embedded silver nanoparticles, J. Non. Cryst. Solids. 498 (2018) 395–400, https://doi.org/10.1016/j.jnoncrysol.2018.03.019.
[20] M.M. Martins, L.R.P. Kassab, D.M. da Silva, C.B. de Araújo, Tm^{3+} doped Bi_2O3-GeO_2 glasses with silver nanoparticles for optical amplifiers in the short-wave-infrared-region, J. Alloys Compd 772 (2019) 58–63, https://doi.org/10.1016/j.jallcom.2018.08.146.
[21] D.E. Hagan, B. Torres-Kulik, A.P. Knights, Post-fabrication trimming of silicon ring resonators via integrated annealing, IEEE Photon. Technol. Lett. 31 (2019) 1373–1376, https://doi.org/10.1109/LPT.2019.2927323.
[22] T. Lange, W. Njoroge, H. Weis, M. Beckers, M. Wuttig, Physical properties of thin GeO_2 films produced by reactive DC magnetron sputtering, Thin Solid Films 365 (2000) 82–89, https://doi.org/10.1016/S0040-6090(99)01106-2.
[23] Z. Yin, B.K. Garside, Low-loss GeO_2 optical waveguide fabrication using low deposition rate rf sputtering, Appl. Opt. 21 (1982) 4324–4328.
[24] A. Chiasera, C. Macchi, S. Mariazzi, S. Valligatla, S. Varas, M. Mazzola, N. Bazzanella, L. Lunelli, C. Pederzolli, D.N. Rao, G.C. Righini, A. Somoza, R. Brusa, M. Ferrari, M.J.F. Digonnet, S. Jiang (Eds.), Eds., 2014, p. 89820D, , https://doi.org/10.1117/12.2042099.
[25] V.D. Del Cacho, D.M. da Silva, L.R.P. Kassab, A.L. Siarkowski, N.I. Morimoto, PbO–GeO_2 rib waveguides for photonic applications, J. Alloys Compd. 509 (2011) S434–S437, https://doi.org/10.1016/j.jallcom.2011.01.141.
[26] F.A. Bomfim, D.M. da Silva, L.R.P. Kassab, T.A.A. de Assumpção, V.D. Del Cacho, M.I. Alayo, Advances on the fabrication process of Er^{3+}/Yb^{3+}:GeO_2–PbO pedestal waveguides for integrated photonics, Opt. Mater. (Amst) 49 (2015) 196–200, https://doi.org/10.1016/j.optmat.2015.09.010.
[27] C. Ba, S.T. Bah, M. D'Auteuil, P.V. Ashrit, R. Vallée, Fabrication of High quality VO_2 thin films by ion-assisted dual AC magnetron sputtering, ACS Appl. Mater. Interfaces 5 (2013) 12520–12525, https://doi.org/10.1021/am403807u.
[28] H. Kupfer, R. Kleinhempel, F. Richter, C. Peters, U. Krause, T. Kopte, Y. Cheng, High-rate deposition of MgO by reactive AC pulsed magnetron sputtering in the transition mode, J. Vac. Sci. Technol. A Vacuum, Surfaces, Film 24 (2006) 106–113, https://doi.org/10.1116/1.2138717.
[29] S.T. Bah, C.O.F. Ba, M. D'Auteuil, P.V. Ashrit, L. Sorelli, R. Vallée, Fabrication of TaO_xNy thin films by reactive ion beam-assisted ac double magnetron sputtering for optical applications, Thin Solid Films 615 (2016) 351–357, https://doi.org/10.1016/j.tsf.2016.07.055.
[30] K. Strijckmans, R. Schelfhout, D. Depla, Tutorial: hysteresis during the reactive magnetron sputtering process, J. Appl. Phys. (2018) 124, https://doi.org/10.1063/1.5042084.
[31] S. Berg, T. Nyberg, Fundamental understanding and modeling of reactive sputtering processes, Thin Solid Films 476 (2005) 215–230, https://doi.org/10.1016/j.tsf.2004.10.051.
[32] M. Mayer, SIMNRA user's guide, Max-Planck-Institut Fur Plasmaphys. (1997).
[33] J.A. Wollam Co. Inc, Complete ease data analysis manual, (2011) 1–207.
[34] I. Horcas, R. Fernández, J.M. Gómez-Rodríguez, J. Colchero, J. Gómez-Herrero, A.M. Baro, WSXM: a software for scanning probe microscopy and a tool for nanotechnology, Rev. Sci. Instrum. (2007) 78, https://doi.org/10.1063/1.2432410.
[35] K.D. Simmons, G.I. Stegeman, B.G. Potter, J.H. Simmons, Photosensitivity of sol-gel-derived germanosilicate planar waveguides, Opt. Lett. 18 (1993) 25–27, https://doi.org/10.1007/978-3-642-78166-7_3.
[36] M. Takahashi, A. Sakoh, Y. Tokuda, T. Yoko, J. Nishii, H. Nishiyama, I. Miyamoto, Photochemical process of divalent germanium responsible for photorefractive index change in GeO_2–SiO_2 glasses, J. Non. Cryst. Solids. 345–346 (2004) 323–327, https://doi.org/10.1016/j.jnoncrysol.2004.08.037.
[37] C.M. Herzinger, B. Johs, W.A. McGahan, J.A. Woollam, W. Paulson, Ellipsometric determination of optical constants for silicon and thermally grown silicon dioxide via a multi-sample, multi-wavelength, multi-angle investigation, J. Appl. Phys. 83 (1998) 3323–3336, https://doi.org/10.1063/1.367101.
[38] S.J. Stefan Jakobs, M.L. Marc Lappschies, U.S. Uwe Schallenberg, O.S. Olaf Stenzel, S.W. Steffen Wilbrandt, Characterization of metal-oxide thin films deposited by plasma-assisted reactive magnetron sputtering, Chinese Opt. Lett. 8 (2010) 73–77, https://doi.org/10.3788/COL201008S1.0073.